



Spatial–Temporal Evolution of a Radial Plasma Jet Array and Its Interaction with Material

Ruixue Wang¹ · Hui Xu¹ · Yong Zhao¹ · Weidong Zhu³ · Cheng Zhang^{1,2} · Tao Shao^{1,2}

Received: 18 July 2018 / Accepted: 13 September 2018 / Published online: 26 September 2018
© Springer Science+Business Media, LLC, part of Springer Nature 2018

Abstract

This paper investigates the behavior of a radial plasma jet array and its interaction with various cylindrical targets. The jet array comprises six individual plasma jets arranged around a circle at even spaces, directed towards a common central axis, where the cylindrical objects are to be treated. The interaction of the six jets without the target is studied. The effect of pulse rise time on the electrical and optical properties of the plasma jets is investigated. The spatial–temporal evolution of the plasma jet array and its interaction with (1) dielectric target, (2) floating metallic target and (3) grounded metallic target, are studied respectively. It is calculated that the velocity of the ionization front in these three cases, although differs amongst themselves, is in general greater than that in the no-target case. The luminosity and the profile of the ionization wave front are noticeably different in these three cases: comparing to the no-target case, the intensity of the ionization front reduces with the presence of a dielectric target, while the luminosity of the ionization wave front is enhanced with the presence of a metallic target (either floating or grounded). Optical emissions at the quartz nozzle exit and at the central axis are different with different targets. The different behavior of the jet array with the presence of different targets is attributed to the local electric field distribution, which will be discussed in this paper.

Keywords Radial plasma jet array · Ionization wave front · Dielectric target · Metallic target · Optical emission

Introduction

Atmospheric pressure plasma processing techniques are of great interest because they are very effective to modify the material surface under mild condition and more importantly, without changing the bulk properties [1, 2]. Atmospheric-pressure plasma jets (APPJs) have drawn much attention due to their compact sizes, high efficiency, low cost and

✉ Tao Shao
st@mail.iee.ac.cn

¹ Institute of Electrical Engineering, Chinese Academy of Sciences, Beijing 100190, China

² University of Chinese Academy of Sciences, Beijing 100049, China

³ Department of Applied Science and Technology, Saint Peter's University, Jersey City, NJ 07306, USA

flexibility. Since APPJs are generated in open air rather than in confined discharge chambers, there is technically little limitation for the object's geometrical dimensions [3–5]. The applications of APPJs have been extended to many areas such as healthcare [6–9], nanotechnology [10–12], chemical conversion [13, 14], material modification [15, 16] and agriculture [17]. With rapid scans of APPJs along the surface, even irregularly shaped objects or complex structures can be modified homogeneously.

One of the drawbacks of a single plasma jet is its small footprint, making it difficult for large-scale industrial applications. Many researchers have tried to group several individual APPJs together to increase the effective treatment area [18–20]. For example, Nie et al. [21] developed a 1-D plasma jet array with jets arranged side-by-side along a line; Sun et al. [22] constructed a 2-D plasma jet array with honeycomb configuration. Robert et al. [23] observed multi-jets splitting in the dielectric tube orifices of a single jet. It should be noted that in a plasma jet array, the interaction between adjacent plasma jets is sometimes non-negligible. Charged particles in the discharge channel introduce a strong repulsive force and cause a divergence in the plasma jets' trajectories [23–26]. Our group have reported the cross-talks of plasma jets in a 1-D microsecond pulse driven argon plasma jet array, and achieved uniform plasma jets at certain gas flow rate and electrode configuration [27]. In a different study by Kim et al. [28, 29] intense and energetic discharge mode that combines nearby plasma jets have been observed under high gas flow rate.

Plasma material processing involves the interaction between a plasma jet (or jet array) and a target to be treated (either dielectric or conductor). When the plasma jet touches the target material, the behavior of the plasma jet could be further complicated. In many cases, the target changes the electrical properties of the plasma jet [30–32]. With a grounded electrode placed downstream of the plasma jet, the discharge mode changes from positive corona mode to dielectric-barrier discharge (DBD) mode upon the streamer touching the target [33]. When a dielectric target is used, charge accumulation occurs on the target surface. The accumulated charges restrict the material deposition rate [34]. As reported by Norberg et al. [35], the different behavior of plasma jet when touching the dielectric or metallic target is due to the difference of permittivity of the materials. Dielectric material with low values of relative permittivity has a large impedance compared to metallic material, thereby increasing the voltage across the electrode-to-target gap. The streamer velocity and electric field increased when moving from dielectric to conductive target. Besides, dielectric material encourages the propagation of electric field along material surface and the formation of surface ionization wave, while metallic material with infinite permittivity promotes the restrike of the ionization wave and the formation of a conduction channel.

Aside from the electrical property, plasma chemistry also varies among different targets. Urabe et al. [36] first observed that He metastables concentration increases with presence of a metallic target. Ries et al. [37] found that the optical emission intensity of OH increased by a factor of five with the presence of a grounded metallic target. Robert et al. [38] confirmed that a secondary ionization front rapidly propagates from the metallic target surface to the inner electrode of the plasma device and is responsible for the higher intensity of He metastables.

This work develops a radial plasma jet array for cylinder subject treatment, which allows a higher treatment area and throughput. The interaction between free jets array and its interaction with either a conductive or a dielectric cylindrical target is studied. More specifically, six individual plasma jets are radially arranged in a circle with the tips of the plasma jets pointing towards the center. This paper is divided into two parts: (1) The effect of pulse rise time on the behavior of the jet array without the presence of the targets and (2) jet array interaction with different targets (dielectric target, floating or grounded metallic

target). The electrical properties, optical properties, spatial–temporal evolution of the radial plasma jet array are investigated.

Experimental Set-Up

The radial plasma jet array comprises six individual plasma jets, each positioned at the center of a side of an insulating hexagon frame to form a circle, with the jets pointing toward the center. Each individual plasma jet utilizes a typical needle-ring electrode configuration, which has been described in detail in our previous work [39]. In order to study plasma-material interaction, a cylindrical target (dielectric or metallic, either floating or grounded) was placed at the center of the hexagon frame and subsequently interacted with the plasma jet array. Research grade argon gas (99.999%) was introduced to a gas diffusion device and then divided into six identical branches to feed six stainless needles (hollow). The overall gas flow rate was controlled by a mass flow controller (Omega, FMA-1607) and was kept at 4 L/min throughout the experiments. The plasma jets were driven by a single pulse generator (Xi'an Smart Maple Electronic Technology, HV-2015) with parameters adjusted in a wide range: voltage amplitude up to 20 kV, pulse rise time between 50 and 500 ns and pulse repetition frequency (PRF) up to 5 kHz at 20 kV. When the plasma jet array was under stable operation, the input voltage was kept at 10 kV and the pulse repetition frequency at 2 kHz. No ballasting resistors were used in the electrical circuit.

The voltage and current characteristics were monitored by a high voltage probe (Tektronix, P6015A, 1000:1) and a current monitor (Pearson, 4100, 1 V/A), respectively, through a digital oscilloscope (Lecory, WR204Xi). The time averaged images were taken by Canon camera (EOS 500D) coupled with Tamron lens (Model A001), with an exposure time of 0.1 s. The spatial–temporal evolution of the ionization wave front of the plasma jets was investigated by using an optical emission spectrometer (Andor, SR-500I) together with an ICCD camera (Andor, DH334T-18U-03). The ICCD camera was synchronized with the jet array via a pulse modulator. The electrical property, spatial–temporal distribution of the ionization wave front, emission of the N_2 second positive system (with band head at 337.1 nm), and the emission of Ar at 763.5 nm were studied and compared under the following four situations: without target, with dielectric target, with floating metallic target and with grounded metallic target (Fig. 1).

The Effect of the Pulse Rise/Fall-Time on the Jet Array Without the Presence of a Target

The Electrical Property

The over-voltage breakdown caused by short pulse rise time is essential for high speed propagation of ionization wave front [40]. The interaction of the six plasma jets under different pulse rise/fall-times was investigated. It was found that the plasma jets do not combine at the center when the distance between the exit nozzles of the quartz tubes and the center (refers to as the Q-C distance) was greater than 10 mm. The interaction of the six jets was therefore studied with the Q-C distance set at 10 mm with various pulse rise/fall-time. The applied voltage pulse typically has the same rise and fall time with duration of 500 ns at its peak (10 kV). Figure 2 shows the waveforms of the discharge voltage and

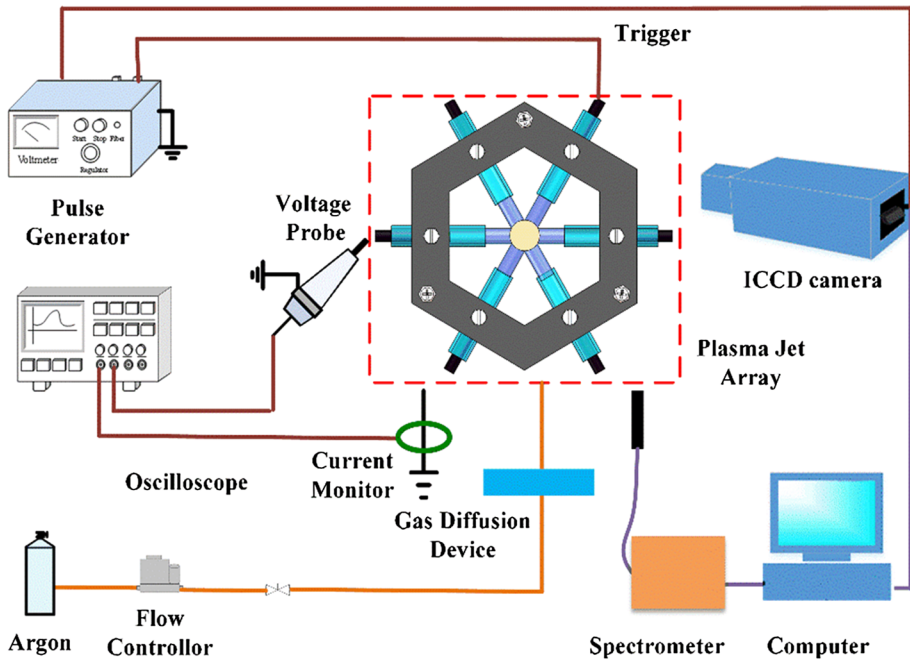


Fig. 1 A schematic diagram of the experimental setup (Color figure online)

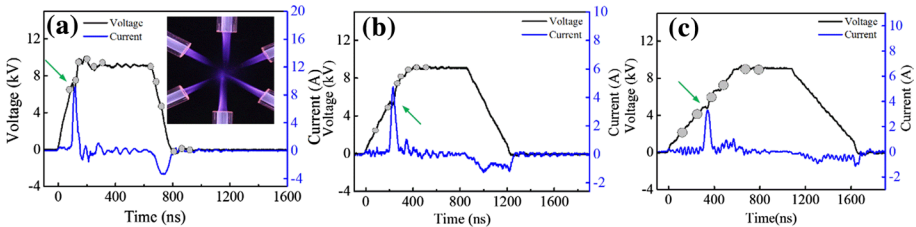


Fig. 2 Voltage and current waveforms with different pulse rise/fall-time: **a** 160 ns, **b** 360 ns and **c** 580 ns (The grey circles on the voltage curve represent the time instants at which the ICCD images were taken; the inset in **(a)** is an exemplary image of the radial jet array)

the discharge current with different rise/fall-times of the pulse. The inset image in Fig. 2a shows the six plasma jets touching each other at the central spot. The discharge currents shown here were calculated as the difference between the total current and the displacement current (with no plasma jets ignited). With a pulse rise/fall-time of 150 ns, 360 ns and 580 ns, the pulse rise/fall rates (defined as dV/dt) were calculated to be 0.067 kV/ns, 0.028 kV/ns and 0.017 kV/ns, respectively. As shown in Fig. 2a, with a pulse rise/fall-time of 150 ns, two discharge current peaks are observable, with a positive discharge at the rising edge and a negative discharge at the falling edge, respectively. The peak value of the negative discharge current (3.3 A) is much smaller than that of the positive (8.8 A). When the pulse rise/fall-time is increased to 360 ns (Fig. 2b), the positive current peak decreased to 4.7 A, and at the same time, the amplitude of negative current also reduced. A similar phenomenon was observed with a pulse rise/fall time of 580 ns (Fig. 2c), but with a much

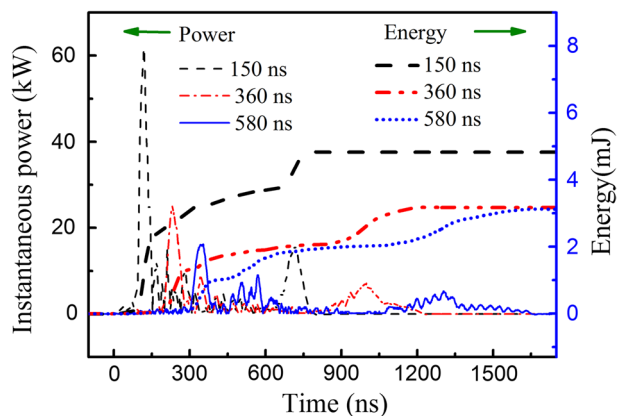
smaller positive current peak. The negative discharge was due to charge accumulation during the primary positive discharge [41]. With a smaller pulse rise rate, the weaker positive discharge lead to less charge accumulated on the quartz tube. Besides, the longer falling edge would further make the reverse breakdown impossible [42]. A bigger pulse rise rate brought forward the discharge time, but with a higher breakdown voltage.

The corresponding instantaneous power and energy under different pulse rise/fall-time: 150 ns, 360 ns and 580 ns are shown in Fig. 3. The instantaneous power and energy were calculated as 61.9 kW, 24.9 kW and 15.8 kW, 4.8 mJ, 3.2 mJ and 3 mJ for pulse rise/fall-time of 150 ns, 360 ns and 580 ns, respectively. The bigger pulse rise/fall time provide a much higher instantaneous power and energy than that of small pulse rise/fall time.

Spatial–Temporal Distribution of the Ionization Front

An ICCD camera was used to capture the dynamics of the discharge to investigate the interaction of the jets in the jet array. Figure 4 shows six false-color photographs of the discharge taken at different delay time during a pulse rise time of 150 ns. Each photograph is an integration of 40 images (gate time: 15 ns) with the same delay time. The discharge outside of the quartz tube resembled a cathode-directed streamer-like discharge, which propagated from the quartz tube to the central spot. The interaction zone is defined as the circular area surrounded by the six quartz nozzles (represented by a red circle in Fig. 4a). The ionization wave fronts of the six plasma jets were almost synchronized and met each other before 180 ns. At the beginning of the discharge, the plasma jets appear to have “flat head” due to the repulsion caused by charged particles, which was totally different from the “arrow head” observed in a single jet [43, 44]. The charges in adjacent streamer channels repel each other, transferring momentum to the neutrals and leading to a horizontal velocity component (velocity component perpendicular to the plasma bullet propagation trajectory) to the propagation trajectory [25]. The six plasma jets eventually combine to one luminous spot at the center (referred to as the “central spot plasma”). The central spot plasma lasted almost 100 ns (Fig. 4d–f) even after the six plasma jets completely diminished at around 300 ns. Our previous studies showed that, with a positive polarity pulse, local electric field in the head of the plasma jet was enhanced by space charges in the discharge channel [45]. The accumulative effect of the local electric field (axial electric field at the plasma plume propagation trajectory direction) from the six plasma jets at the central

Fig. 3 The calculated instantaneous power and energy under different pulse rise/fall-time: **a** 150 ns, **b** 360 ns and **c** 580 ns (Color figure online)



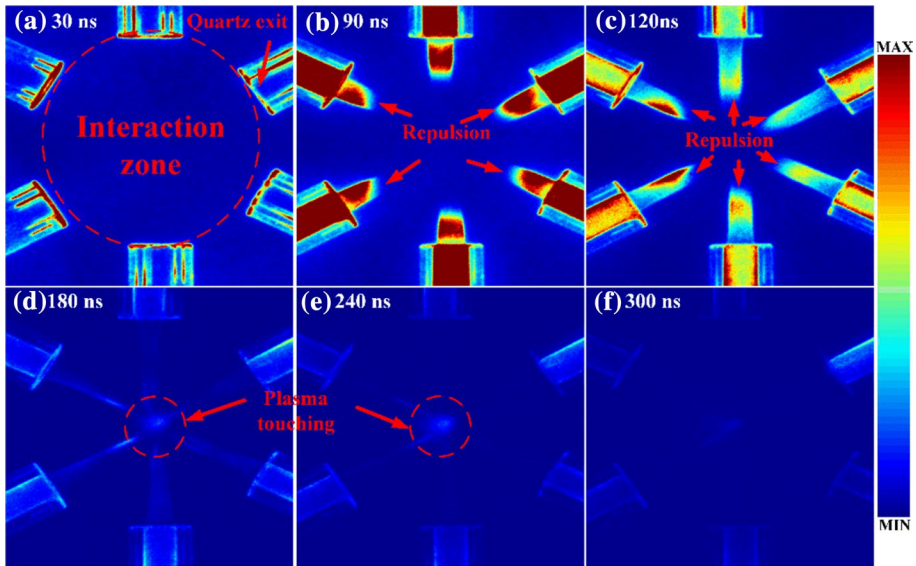


Fig. 4 Dynamic studies of the interaction of the six plasma jets during the positive discharge (gate width: 15 ns, accumulation: 40, gain level: 2000) (Color figure online)

spot can maintain the central spot plasma for a long time. Figure 5 shows the dynamic evolution of the plasma jet array during the negative discharge. As we can see, the discharge was mainly located inside the quartz tube. Very weak plasmas appeared outside the quartz tubing at 690 ns. No obvious discharge was observed in the interaction zone afterwards.

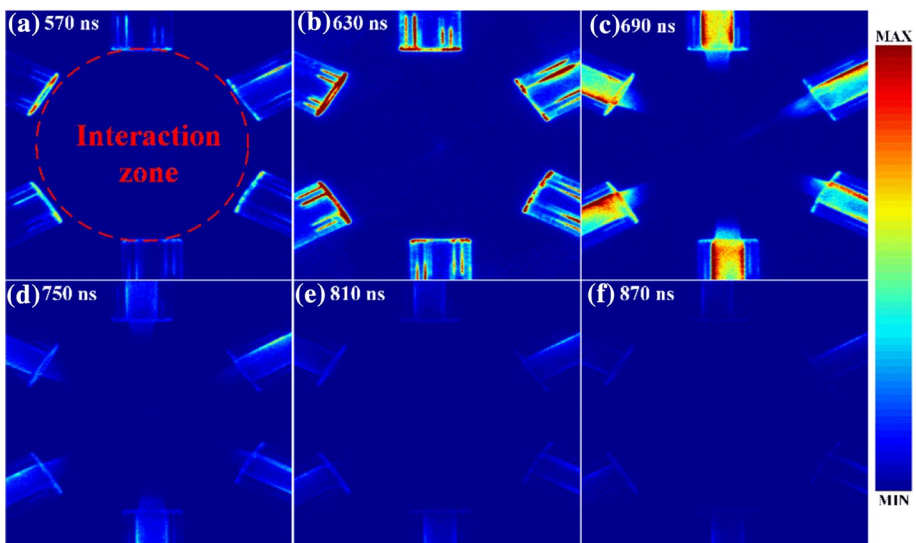


Fig. 5 Dynamic studies of the interaction of the six plasma jets during the negative discharge (gate width: 15 ns, accumulation: 40, gain level: 2000)

The weak discharge current at the falling edge cannot afford the ionization wave fronts to travel a long distance. The rest of this study will be focused on only the positive discharge.

The dynamics of the plasma jet array under longer pulse rise time (360 and 580 ns) is shown in Fig. 6. The discharge began at 90 ns (not shown in figure) with a pulse rise time of 360 ns. When the pulse rise was increased to 580 ns, the start time of the discharge is further delayed. This is in agreement with the discharge current waveforms as shown in Fig. 2. It should be noted that with the increase of the pulse rise-time, the plasma jets meet at the center (forming a central spot plasma) at a later time. The central spot plasma was formed at 180 ns, 300 ns and 360 ns with pulse rise-time of 150 ns, 360 ns and 580 ns,

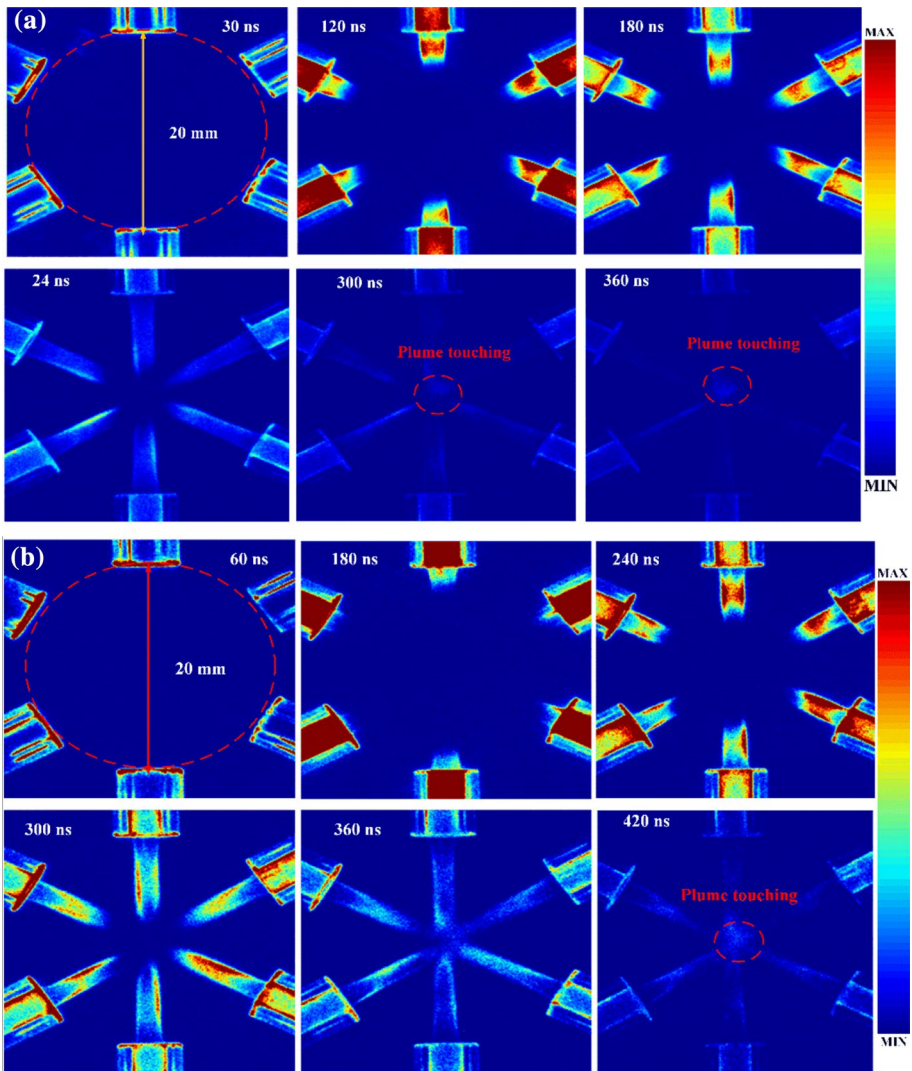


Fig. 6 Dynamic studies of the interaction of the six plasma jets with a pulse rise-time of **a** 360 ns and **b** 580 ns

respectively. Strictly speaking, the central spot plasma was a little off-centered, due to the imperfect arrangement of our jet array. A slightest difference between neighboring jets may lead to a difference in their propagation time, and in turn the location where they meet.

The Interaction of the Plasma Jet Array with Different Targets

Electrical Characterization

Placing different targets at the center of the interaction zone alters the discharge properties of the plasma jet array. The following four situations were involved in this study: (A) no target, (B) with dielectric target, (C) with floating metallic target and (D) with grounded metallic target. A solid cylindrical stainless steel tube (diameter: 3 mm) and polyethylene tube (diameter: 4 mm) were used as metallic and dielectric targets, respectively. The distance between the exit nozzles of the quartz tubes and the outer surface of the target (referred to as the Q-T distance) was 30 mm. All experiments were conducted with a pulse rise-time of 150 ns. Figure 7 shows the images of the plasma jet array of the aforementioned four cases. For the no-target case, at a Q-T distance of 30 mm, the plasma jets do not combine at the center, i.e. no central spot plasma was observed (Fig. 7a). In the cases of dielectric target and floating metallic target, the discharges between the exit nozzles of the quartz tubes and the target show no obvious difference with the no target situation (Fig. 7b, c). However, a closer observation of the target surface revealed bright diffused discharge spots on the surface of the dielectric target (see inset in Fig. 7b). Similar surface discharge was also observed on the floating target, but more localized (see inset in Fig. 7c). A very bright spindle-shaped discharge channel appeared between the quartz tubes and the grounded metallic target (Fig. 7d). The plasma jets seem to become weaker when propagating away from the quartz tubes, and are then enhanced when touching the grounded metallic target. The enhanced discharge channels are much thicker. This is probably due to the ionization wave restrike, which will be discussed later.

The discharge voltage and current were also monitored with the presence of different targets. It should be noted that typically two types of currents are of concern: (1) the discharge current between the high voltage electrode and the ground electrode and (2) current carried by the plasma jets. In this study, only the former current was monitored. The later current is hard to monitor in this case due to the size of our current monitor and the limited space at the center of the hexagon frame. As we can see from Fig. 8, the existence of targets, or the targets properties had no obvious influence on the time of the appearance or the amplitude of the discharge current between high voltage and ground electrode, which means that the existence of targets may only change the discharge properties between the quartz tubes and the target. Similar result has been obtained by Guaitella et al. [46].

Spatial–Temporal Distribution of the Ionization Wave Front

The dynamic distribution of the ionization wave front of the plasma jets was further investigated through an ICCD camera to understand the plasma-target interaction. Figure 9 shows the time evolution of the jet array under the four situations as described in Sect. 4.1. After applying voltage, an ionization wave was initiated from the high voltage electrode and propagated through the argon channel inside the quartz tube, out of the tube into the ambient air. In situations (B), (C), (D), the ionization wave further struck the surface of the

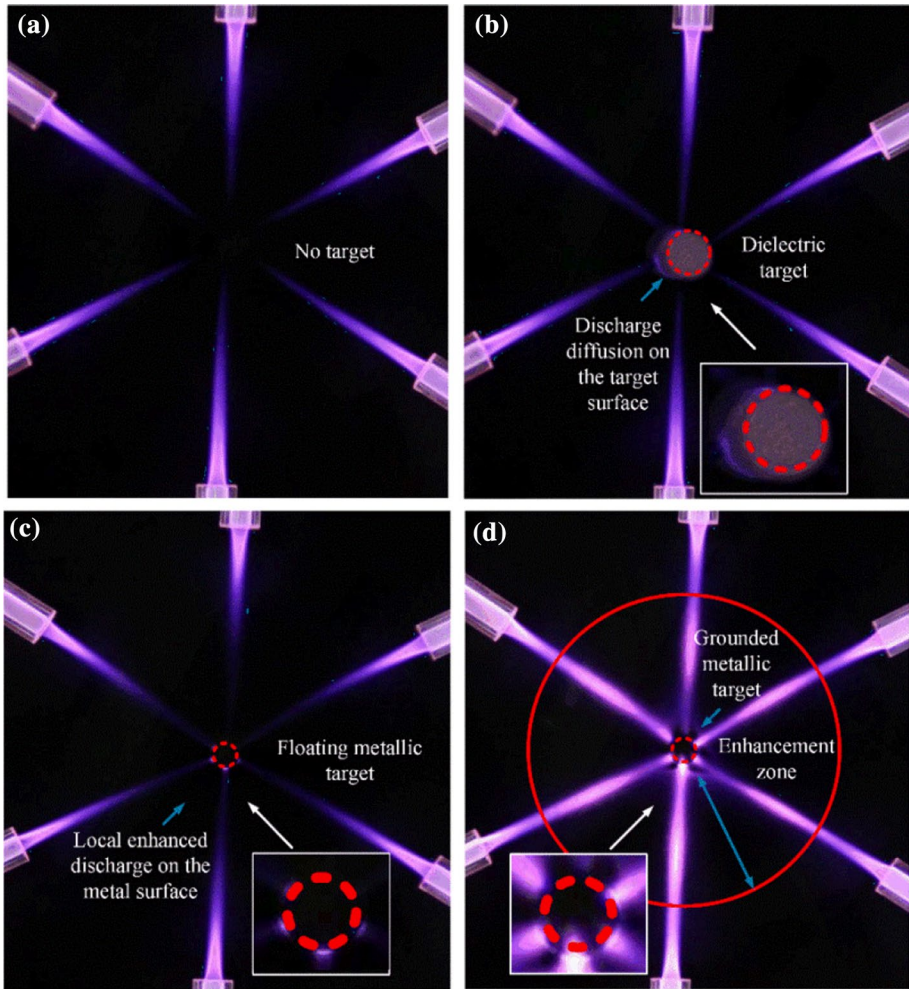


Fig. 7 The discharge images with different targets: **a** no target, **b** dielectric target, **c** floating metallic target and **d** grounded metallic target; Insets show closeup views of the target surface

target. Four close-up images are shown in Fig. 10 to illustrate the interaction of the plasma jets (with the targets) near the center. With a positive pulse, the electrons moved toward to the anode and accumulated on the dielectric material surface [47]. Positive ions in the front of the streamer moved slowly due to their high masses and formed an opposite space electric field. The space electric field enhanced the local electric field in the streamer head and generated an electron avalanche. The impact of electrons in the discharge ionization front and inner capillary wall charging processes are critical for the ionization wave front propagation [41]. With the propagation of the streamer, the electric field decreased. The discharge became weak and finally disappeared at 270 ns (Fig. 9a). With a longer Q-C distance of 30 mm, there is no jet repulsion observed.

With dielectric target (Fig. 9b), the ionization wave front of the six plasma jets show lower luminous intensity when compared to those at the same time frame in the

Fig. 8 The current waveform of the plasma jet array with different targets

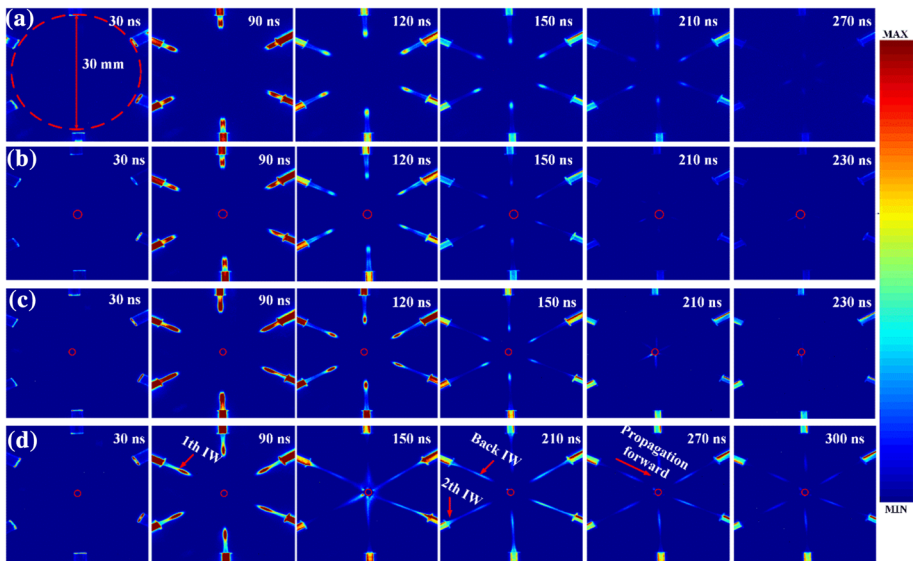
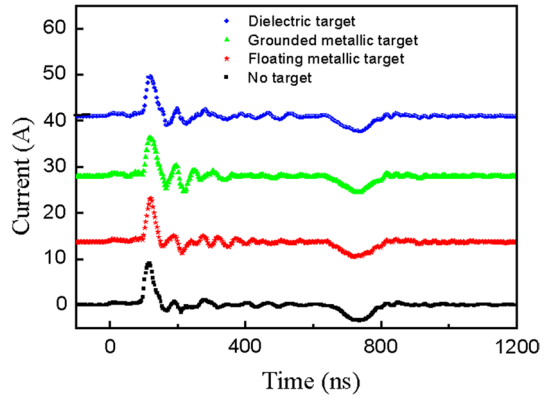


Fig. 9 The dynamic evolution of the plasma jet array: **a** no target, **b** with dielectric target, **c** with floating metallic target and **d** with grounded metallic target (The solid circles in **b–d** outline the boundary of the targets) (Color figure online)

no target situation. The existence of the dielectric target can be considered as adding a small capacitor in the electrical circuit. When the ionization front touched the dielectric target, charges in the ionization front moved to the dielectric material surface and were captured by surface charge traps. These charges can be transported into the material's bulk or conducted along the material's surface [48]. The amount of injected charges is determined by the properties of the ionization wave and the intrinsic characteristics of the dielectric material, i.e. trap number, trap level distribution and permittivity [49]. Large trap number and deep trap level help charge capture, while high values of relative permittivity reduce the charge accumulation on the material surface. After charging, a horizontal component of the electric field along the dielectric target was formed.

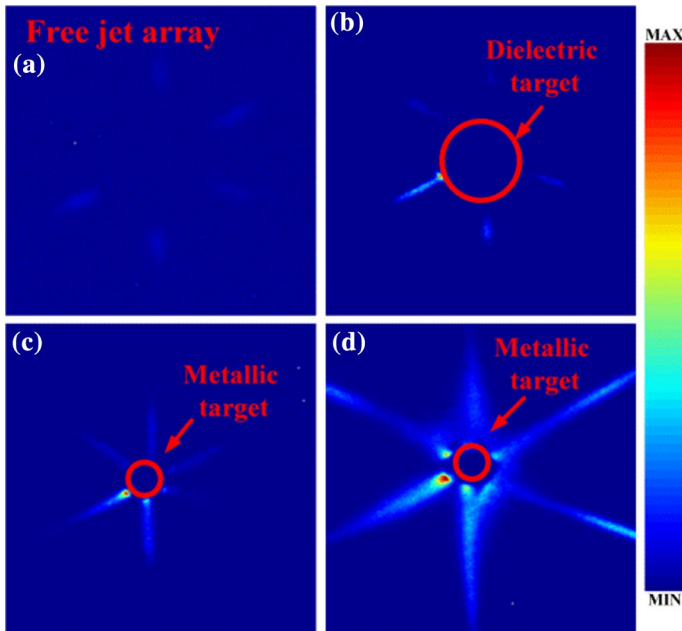


Fig. 10 A close-up view of the jet array and target interaction: **a** no target, **b** with dielectric target, **c** with floating metallic target and **d** with grounded metallic target

The formation of the horizontal electric field was at the expense of the vertical electric field. The smaller voltage across the gap results in the lower luminous intensity streamer head. Normally, a new small ionization wave generated by the horizontal electric field is observed along the dielectric target [35]. In our case, the six streamer heads did not reach the surface of the dielectric target simultaneously due to the slight variation of the Q-T distances. Only the first streamer arrived at the dielectric target seemed to spread slightly on the surface (Fig. 10b). The large Q-T distance (30 mm) caused the overall electric field to be small at the target surface and the horizontal electric field caused by charge accumulation is limited. Furthermore, the curvature of the dielectric target makes the diffusion of the plasma more difficult when compared to planar objects.

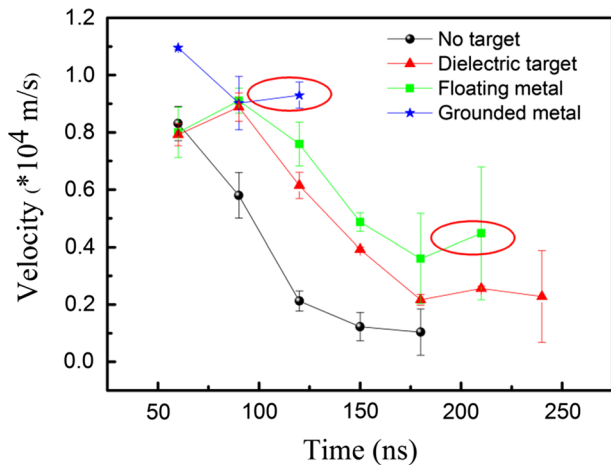
With floating metallic target, the ionization wave front travelled at a faster velocity than in the dielectric target case. It is also interesting to note that the six ionization wave fronts reached the target simultaneously at 210 ns. The luminous intensity of one of the jets appears to be stronger than that of the others (Fig. 10c), again likely due to the slight variation of the Q-T distances. The existence of grounded metallic target reduced the repulsion force between adjacent jets, the ionization wave front presented typical “arrow shape” of single jet. When the ionization wave front touched the target, a spark-like discharge was formed on the target surface. The difference between the floating metallic target and the dielectric target is their permittivity. The floating metallic target can be considered as a target with infinite permittivity. When coming in contact with the floating metallic target, charges in the ionization front were neutralized by free electrons in the metallic target. The metallic target was charged to the same amount of charges as the ionization front, but without consuming the vertical electric field. The spark discharge may be due to both the local electric field and micro defects on the surface of the metal: The local electric field due to

charges alone may not be strong enough to cause a spark discharge on the metal surface. However, micro defects (in most of the cases) exist on the metal surface, which will cause strong electric field distortion, and in turn a spark discharge.

In the case of grounded metallic target, the ionization wave fronts of the six plasma jets travelled in a much faster velocity and simultaneously reached the target at 150 ns (Fig. 9d). The ionization wave front extended on the target surface and combined with each other, forming a circular discharge around the metallic surface. The circular discharge coexists with several bright spark-like and diffused discharge (Fig. 10d). After touching the metallic target, the ionization wave front reversed its direction and propagates towards the quartz tubing. With a grounded metal target, there was no charging of the surface and the full voltage remained across the discharge channel. The high electric field across the discharge channel can sustain a highly conductive ionized channel, which allows the secondary and back ionization wave fronts travelling inside. At 210 ns, the secondary ionization wave front overlapped with back ionization wave front, together induced a high discharge intensity in this area, which corresponds to the spindle-shaped discharge channel in Fig. 7. The overlapped ionization wave front travelled towards to the target and gradually faded until electric field cannot sustain the discharge further (270 and 300 ns).

The velocity of the ionization wave fronts at each condition are calculated and shown in Fig. 11. The velocity here refers to the average velocity of the six plasma jets' ionization wave front. Each data point was measured three times to reduce experimental error. Only the velocity of first ionization front in grounded metallic target case was calculated to be consistent with other conditions (no target, with dielectric target or floating target). The maximum velocity of the plasma ionization wave front in different cases was in the range of $0.8\text{--}1.2 \times 10^4$ m/s, which is in accordance with what's reported in other literatures [50]. The average velocity follows the following order: grounded metallic target > floating metallic target > dielectric target > no target. The existence of metallic target (no matter whether grounded or floating), seem to have a "pulling" effect on the ionization wave front, by increasing the velocity when the ionization front touched metallic target (right circles). The study in this paper provides physical mechanism for surface modification by plasma jet or jet array. In our previous studies, we found that the film deposition rate for plasma-metal modification was ten times higher than that of plasma-dielectric modification. For example, the film thickness on copper surface was several μm , while the film thickness on dielectric surface was 200 nm with similar plasma

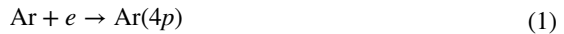
Fig. 11 The average velocity of the ionization wave front under different conditions (secondary ionization front was not considered in this figure) (Color figure online)



parameters [51, 52]. This result is consistent with the intense discharge near the target surface when metallic target was involved. Besides, discharges with different targets also predicted that the grounded metallic target might have a better surface modification effect than that of floating metallic target, which is what has been observed in our prior studies.

Optical Emission

The optical emission was recorded at the exit of the quartz tube and at the central spot to investigate the reactive species generated at these two locations. As shown in Fig. 12a, at the exit of quartz tubing, other than strong argon emissions from 700 to 900 nm, emissions from the N₂ second positive system N₂(C³Π_u → B³Π_g) (refers as N₂(C)) at 337.1 nm, 353.7 nm, and 357.7 nm (refers to N₂ emission), OH emissions at 306–309 nm due to transition [A²Σ⁺ → X²Π(Δν = 0)] were also observed in the spectra. The 620 nm emission is due to the secondary diffraction of N₂ and OH molecule emissions. The Ar emissions are mainly formed by electron impact excitation in the discharge.



The N₂(C) can be generated by electron impact excitation or argon metastables energy transfer. As the metastable states of argon (defines as Ar_m) have energies 11.55 eV (Ar_m 3P²) and 11.72 eV (Ar_m 3P⁰), which are slightly higher than those of N₂(C) excited states, it can be considered that the population of the Ar metastables is lowered through the Ar–N₂ resonance energy transfer:

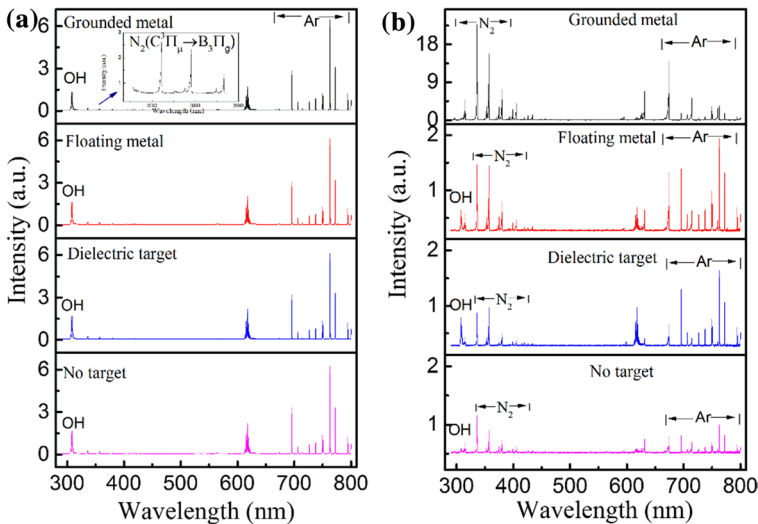
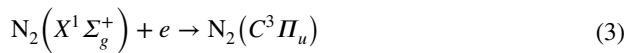
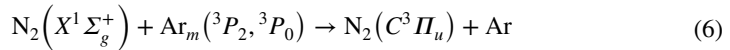
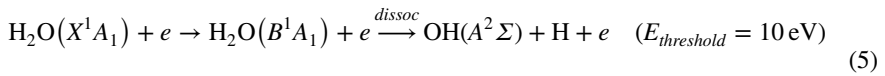
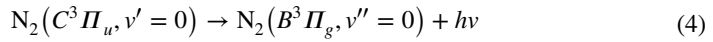


Fig. 12 Optical emission spectra of jets array at **a** the quartz exit nozzle and **b** the central spot (Color figure online)



As we all known, the atomic or molecular emission intensity is linked to the population of upper state level, which is determined by the reaction rate of electron impact fraction and the number density of the ground state molecules or atoms. The Ar ($4p \rightarrow 4s$) (refers to Ar($4p$)) and $\text{N}_2(C^3\Pi_u \rightarrow B^3\Pi_g)$ have a similar excitation potential around 11 eV, but the concentration of argon at the exit of quartz tubing is very high, which resulted in a higher emission intensity. It should be note that there were no noticeable differences on the emission lines and intensity in the four situations, which further confirmed that the existence of targets only had influence on the plasma jets in open air.

At the central spot, the N_2 molecular is abundant due to air diffusion at such a long distance. Although the observable reactive species are the same as at the quartz exit nozzle, the optical emission at the central spot were different from that at the exit nozzle in the following aspects: (1) The overall emission intensity was lower, so we had to double the exposure time; (2) N_2 emission intensity was enhanced in different levels in all four cases and (3) Ar emission intensity with any target at the center also enhanced comparing to the no target case. As the reduced electric field (E/N) at the end of the jet array was very small to sustain the discharge in air, it was reasonable for the low emission intensity at this location. The existence of dielectric target created a horizontal electric field, which was responsible for Ar emission intensity increase (40%). The increase of Ar emission indicated that electron with relatively lower energy was created in this case. As for the floating metallic target case, both N_2 and Ar emission increased (21 and 50%, respectively). With the existence of grounded metallic target, the N_2 and Ar emission increased to a much higher level (95 and 74%, respectively). In the dielectric target case, the charge accumulation on the dielectric surface created a horizontal electric field, which was responsible for higher OH, Ar and N_2 emission intensities. Similarly, in the floating metallic target case, the spark-like discharge caused by the charge accumulation and electric field distortion can lead to relatively strong emissions. The high electric field across the discharge channel with the presence of a grounded metallic target can sustain a highly conductive ionized channel and generate high intensity of Ar metastables [41]. The electron impact excitation or energy transfer from Ar metastable to ground state N_2 generated abundant excited state N_2 molecules, resulting in high N_2 emission in ground metallic target case.

The temporal evolution of Ar emission (763.5 nm) and N_2 emission (337.1 nm) at the quartz exit nozzle and the central spot were investigated and the results are shown in Figs. 13 and 14, respectively. Two argon emission peaks appeared during one pulse period, which correspond to the positive and negative discharges at the rising and falling edges of the pulse. The argon emission appeared simultaneously with discharge current (Fig. 13a) and reached their peaks at 110–150 ns and at 710–740 ns, respectively, coinciding with the positive and negative current peak. The Ar emission decayed rapidly as the current decrease (No target, Dielectric target and Floating metallic target case). This indicates that the Ar ($4p$) was mainly generated by electron impact excitation. With the existence of grounded metallic target, the Ar emission sustained a relatively high intensity even when there was no discharge current. This was due to the strong ionization channel between the

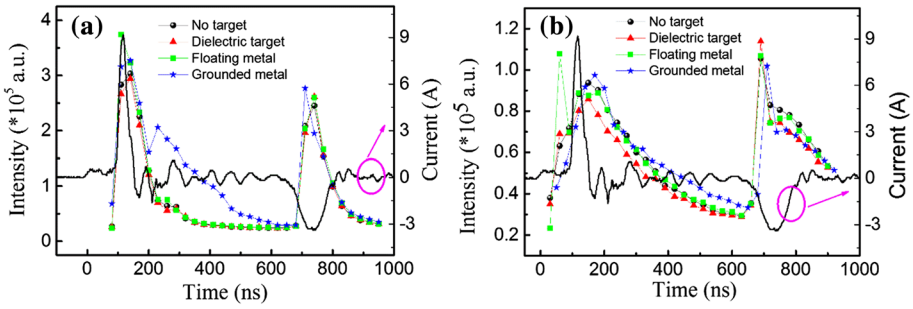


Fig. 13 Temporal evolution of the **a** Ar emission and **b** N₂ emission at the quartz exit nozzle (Color figure online)

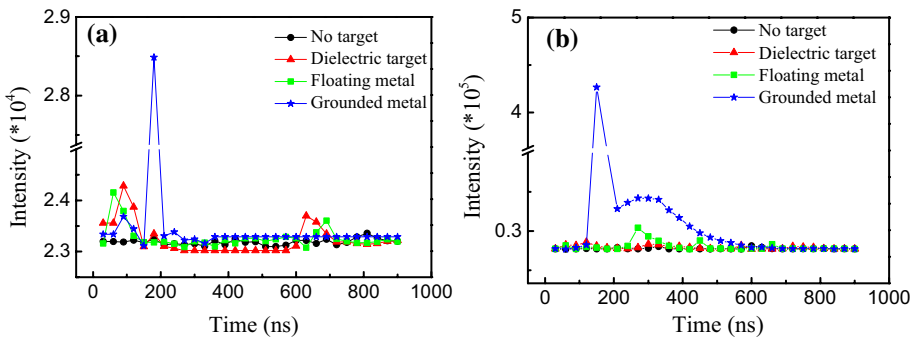


Fig. 14 Time evolution of the **a** Ar emission and **b** N₂ emission at the central spot (Color figure online)

nozzle exit and central spot in this case. The N₂ emission rose simultaneously with the discharge current, but decayed at a slower rate. At the rising edge, electron impact excitation dominated the pathway of N₂ emission. However, at the falling edge, Penning excitation [reaction (6)] and stepwise excitation from excited states of N₂ should be considered [53]. The emission intensity of N₂ emission was weaker than that of Ar emission due to the low gas composition at the exit nozzle area.

In the no target case, no time evolution of Ar or N₂ emissions at the central spot were detected due to the weak discharge intensity (Fig. 14). Ar emission was observed from 0 to 150 ns in the other three cases. At such a Q-T distance, the plasma ionization wave fronts did not travel to the central spot (Fig. 9). As for the grounded metallic target, a strong Ar emission appeared at 180 ns. As we noticed from Fig. 9, the restrike of ionization wave front occurred between 150 ns and 210 ns, which was in the same time scale as the appearance of the Ar emission peak. A secondary Ar emission peak appeared at 630 ns and 690 ns for dielectric target and floating metallic target, respectively, which corresponds to the negative discharges at the falling edge of the pulse. The N₂ emission intensity rose rapidly at 150 ns due to the restrike of ionization wave. The decay rate of N₂ emission was much slower due to the stepwise excitation from the N₂ excited states. A small N₂ emission peak appeared at 270 ns in the floating metallic target case. Similar emission waveforms were observed by Darny et al. [39], the glow like regime around the target surface is favorable to excite N₂(C).

Conclusion

In this paper, the interaction between a coaxial arranged jets array and different targets are studied. Free jets plume touch in the central spot with a quartz nozzle to central spot distance of 10 mm. Obvious jet—jet repulsion is observed due to charged particles in the ionization front. The local electric field is enhanced in the ionization front after jets touching and luminous channel last for 100 ns in the central spot. The short pulse rise time ensures a higher discharge current and makes touching moment in advance. The ionization front luminosity and profile are dependent on the target properties. The velocity of ionization wave front follows the order: free jet array < dielectric target < floating metallic target < grounded metallic target. After touching the grounded metallic target, the ionization front reverses its direction and propagates towards the quartz tubing. Accordingly, the dynamic evolution of Ar emission last for a long time even there is no applied voltage. The existence of targets increases the luminosity at the central spot in different levels: grounded metallic target > floating metallic target > dielectric target. The results obtained in this work is essential for guiding the material surface modification when involved with APPJs.

Acknowledgements This work was supported by the National Natural Science Foundation of China under Contract Nos. 51637010, 51507169, and 11611530681. The authors also want to thanks the supports of State Key Laboratory of Control and Simulation of Power System and Generation Equipments (Tsinghua University) under Contract SKLD17KM06 and Yong Elite Scientists Sponsorship program by CAST (2016QNR001).

References

1. Kogelschatz U (2003) *Plasma Chem Plasma Process* 23:1
2. Shao T, Yang W, Zhang C, Niu Z, Yan P, Schamiloglu E (2014) *Appl Phys Lett* 105:044102
3. Cheng H, Lu X, Liu D (2015) *Plasma Process Polym* 12:1343
4. Wang R, Gao Y, Zhang C, Yan P, Shao T (2016) *IEEE Trans Plasma Sci* 44:393
5. Chen C, Liu D, Yang A, Chen H, Kong MG (2017) *Plasma Chem Plasma Process* 38:89
6. Cheng H, Liu X, Lu X, Liu D (2016) *High Volt* 1:62
7. Zhang Z, Xu Z, Cheng C, Wei J, Lan Y, Ni G, Sun Q, Qian S, Qian S, Zhang H, Xia W, Shen J, Meng Y, Chu PK (2017) *Plasma Chem Plasma Process* 37:415
8. Keidar M, Robert E (2015) *Phys Plasmas* 11:121901
9. Bekešchus S, Favia P, Robert E, Woedtke TV (2018) *Plasma Process Polym.* <https://doi.org/10.1002/ppap.201800033>
10. Duan L, Jiang N, Lu N, Shang K, Li J, Wu Y (2018) *Plasma Sci Technol* 20:054009
11. Ostrikov K, Cvelbar U, Murphy AB (2011) *J Phys D Appl Phys* 44:174001
12. Mavrier F, Zoubian F, Bienia M, Coudert JF, Lejeune M, Rat V, Andre P (2018) *Plasma Chem Plasma Process* 38:657
13. Shao T, Wang R, Zhang C, Yan P (2018) *High Volt* 3:14
14. Yang Y (2002) *Ind Eng Chem Res* 41:5918
15. Wang R, Zhang C, Liu X, Xie Q, Yan P, Shao T (2015) *Appl Surf Sci* 328:509
16. Penkov OV, Khadem M, Lim WS, Kim DE (2015) *J Coat Technol Res* 12:225
17. Brandenburg R, Bogaerts A, Bongers W, Fridman A, Fridman G, Locke BR, Miller V, Reuter S, Schiorlin M, Verreycken T, Ostrikov K (2018) *Plasma Process Polym.* <https://doi.org/10.1002/ppap.201700238>
18. Babaeva NY, Kushner MJ (2014) *Plasma Sour Sci Technol* 23:015007
19. Wang T, Wang X, Yang B, Chen X, Yang C, Liu J (2017) *J Micromech Microeng* 27:075005
20. Zhang P, Wu S, Tan X, Tu Y, Pei X, Gou J, Zhou K, Yang Y (2014) *IEEE Trans Plasma Sci* 42:2460
21. Nie Q, Cao Z, Ren C, Wang D, Kong MG (2009) *New J Phys* 11:115015
22. Sun P, Chen H, Park S, Eden JG, Liu D, Kong M (2015) *J Phys D Appl Phys* 48:425203

23. Robert E, Darny T, Dozias S, Iseni S, Pouvesle (2015) *Phys Plasmas* 22:122007
24. Wan F, Liu F, Fang Z, Zhang B, Wan H (2017) *Phys Plasmas* 24:093514
25. Ghasemi M, Olszewski P, Bradley JW, Walsh JL (2013) *J Phys D Appl Phys* 46:052001
26. Zhou R, Zhang B, Zhou R, Liu F, Fang Z, Ostrikov K (2018) *J Appl Phys* 124:033301
27. Wang R, Sun H, Zhu W, Zhang C, Zhang S, Shao T (2017) *Phys Plasmas* 24:093507
28. Kim JY, Ballato J, Kim SO (2012) *Plasma Process Polym* 9:253
29. Kim JY, Kim SO (2011) *IEEE Trans Plasma Sci* 39:2278
30. Ning W, Dai D, Zhang Y, Han Y, Li L (2018) *J Phys D Appl Phys* 51:125204
31. Bruggeman PJ, Kushner MJ, Locke BR, Gardeniers JGE, Graham WG et al (2016) *Plasma Sour Sci Technol* 25:053002
32. Norberg SA, Johnsen E, Kushner MJ (2016) *J Phys D Appl Phys* 49:185201
33. Kovacevic VV, Sretenovic GB, Slikboer E, Guaitella O (2018) *J Phys D Appl Phys* 51:065202
34. Ito Y, Fukui Y, Urabe K, Sakai O, Tachibana K (2010) *Jpn J Appl Phys* 49:066201
35. Norberg SA, Johnse E, Kushner MJ (2015) *J Appl Phys* 118:013301
36. Urabe K, Morita T, Tachibana K, Ganguly BN (2010) *J Phys D Appl Phys* 43:95201
37. Riès D, Dilecce G, Robert E, Ambrico PF, Dozias S, Pouvesle JM (2014) *J Phys D Appl Phys* 47:275401
38. Darny T, Pouvesle JM, Puech V, Douat C, Dozias S, Robert E (2017) *Plasma Sour Sci Technol* 26:045008
39. Wang R, Zhang K, Shen Y, Zhang C, Zhu W, Shao T (2016) *Plasma Sour Sci Technol* 25:015020
40. Robert E, Sarron V, Ries D, Dozias S, Vandamme, Pouvesle JM (2012) *Plasma Sour Sci Technol* 21:034017
41. Mussard MDVS, Foucher E, Rousseau S (2013) *J Phys D Appl Phys* 48:302001
42. Qian M, Li G, Liu S, Zhang Y, Li S, Lin Z, Wang D (2017) *Plasma Sci Technol* 19:064015
43. Ye R, Zheng W (2008) *Appl Phys Lett* 93:071502
44. Lu X, Laroussi M (2006) *J Appl Phys* 100:063302
45. Wang R, Zhang C, Shen Y, Zhu W, Yan P, Shao T, Babaeva NY, Naidis GV (2015) *J Appl Phys* 118:123303
46. Guaitella O, Sobota A (2015) *J Phys D Appl Phys* 48:255202
47. Boeuf J, Yang L, Pitchford L (2013) *J Phys D Appl Phys* 46:015201
48. Zhang B, Zhang G (2017) *J Appl Phys* 121:105105
49. Kindersberger J, Lederle C (2008) *IEEE Trans Dielectr Electr Insul* 15:941
50. Chen C, Li S, Wu Y, Li Z, Zhang J, Wang Y (2016) *Phys Plasmas* 23:123501
51. Xie Q, Lin H, Zhang S, Wang R, Kong F, Shao T (2018) *Plasma Sci Technol* 20:025504
52. Wang R, Li W, Zhang C, Ren C, Ostrikov K, Shao T (2017) *Plasma Process Polym* 14:e1600248
53. Yi W, Williams P (2002) *J Phys D Appl Phys* 35:205